Electronic Supplementary Material (ESI) for Journal of Materials Chemistry C.
This journal is © The Royal Society of Chemistry 2023

Glassy and liquid Sb_2S_3: insight into the structure and dynamics of a promising functional material

Mohammad Kassem,[a] Chris J. Benmore,[b] Andrey Tverjanovich,[c] Takeshi Usuki,[d] Maxim Khomenko,[e] Daniele Fontanari,[a] Anton Sokolov,[a] Koji Ohara,[f] Maria Bokova,[a] Shinji Kohara,[g] and Eugene Bychkov*[a]

[a] *Laboratoire de Physico-Chimie de l'Atmosphère, Université du Littoral Côte d'Opale, 59140 Dunkerque, France. E-mail: bychkov@univ-littoral.fr*
[b] *X-ray Science Division, Advanced Photon Source, Argonne National Laboratory, Argonne, Illinois 60439, United States*
[c] *Institute of Chemistry, St. Petersburg State University, 198504 St. Petersburg, Russia*
[d] *Faculty of Science, Yamagata University, Yamagata 990-8560, Japan*
[e] *ILIT RAS–Branch of the FSRC "Crystallography and Photonics" RAS, 140700 Shatura, Moscow Region, Russia*
[f] *Research and Utilization Division, Japan Synchrotron Radiation Research Institute, 1-1-1 Kouto, Sayo, Hyogo 679-5198, Japan*
[g] *Quantum Beam Field, Research Center for Advanced Measurement and Characterization, National Institute for Materials Science, 1–2–1 Sengen, Tsukuba, Ibaraki 305–0047, Japan*

Electronic supplementary information

Fig. S1 Raw diffraction patterns of nanocrystalline and glassy Sb_2S_3.

Fig. S2 Raman spectrum of amorphous antimony.

Fig. S3 Evolution of Raman spectra for Sb_2S_3 as a function of temperature.

Fig. S4 DFT Raman spectra of size-limited clusters.

Fig. S5 S-Sb-S bond angle distributions for DFT-optimized clusters.

Fig. S6 Distributions of Sb-S interatomic distances in DFT-optimized clusters.

Fig. S7 High-energy X-ray diffraction data for glassy and liquid As_2S_3.

Fig. S8 Comparison of FPMD modeling with standard PBE and hybrid PBE0 functionals.

Fig. S9 FPMD modeling of glassy As_2S_3 under high-pressure.

Fig. S10 Fitting Sb-S partials with asymmetric functions.

Fig. S11 Coordination distributions of sulfur and antimony.

Fig. S12 Bond angle distributions in glassy and liquid Sb_2S_3.

Fig. S13 FPMD partial pair-distribution functions $g_{\mathrm{PnS}}(r)$ for g-Pn_2S_3, Pn = As, Sb, and experimental $g_{\mathrm{X}}(r)$ for g-As_2S_3 at ambient pressure and 6.3 GPa.

Fig. S14 Derived Sb and S diffusion coefficients plotted on Arrhenius scale.

Fig. S15 FPMD estimation of the SC-M transition temperature $T_{\mathrm{SC-M}}$ for liquid Sb_2S_3.

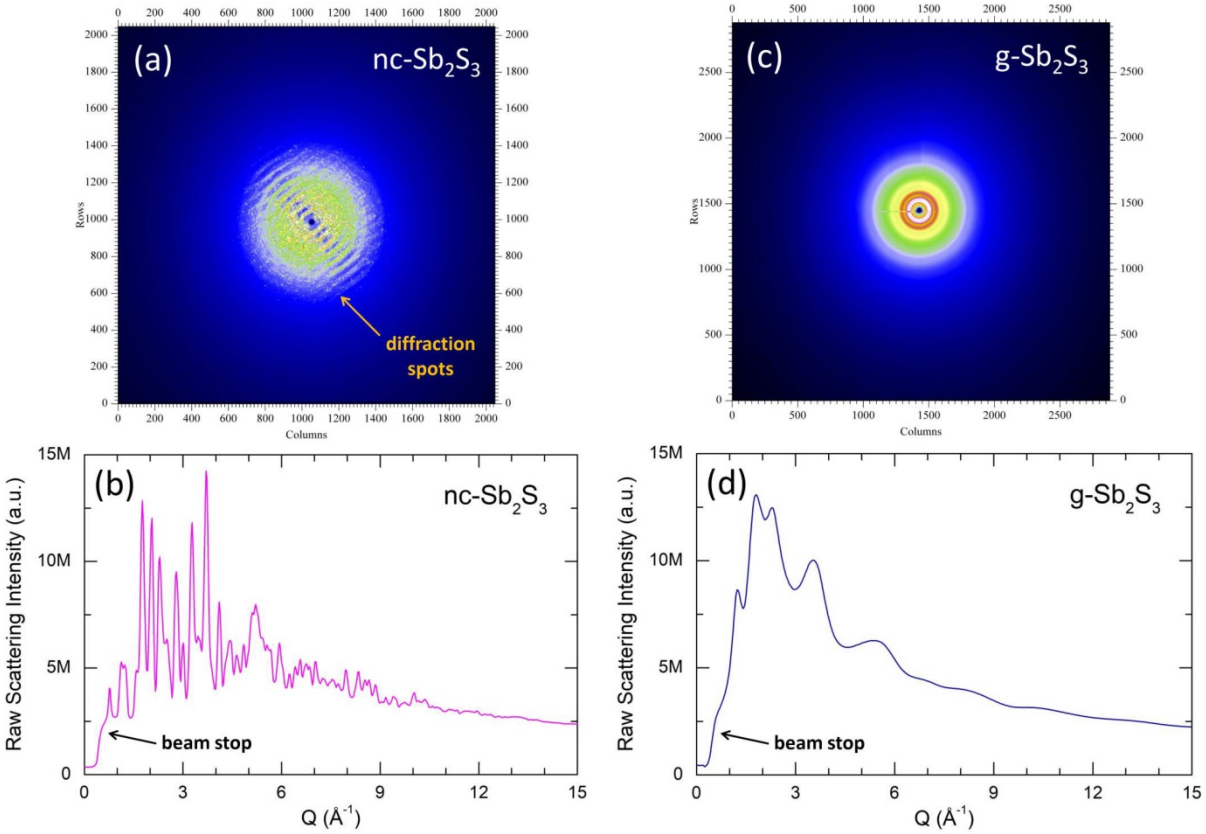

Fig. S1 Raw diffraction patterns of (a,b) nanocrystalline *nc*-Sb_2S_3 and (c,d) glassy *g*-Sb_2S_3 including (a,c) two-dimensional images of the flat high-energy X-ray detectors and (b,d) their radial averaging. A PerkinElmer model 1621 X-ray area detector (2048 × 2048 pixels and a pixel size of 200 × 200 μm²) was used for *nc*-Sb_2S_3, and a Varex area detector (2880 × 2880 pixels and a pixel size of 150 × 150 μm²) for *g*-Sb_2S_3.

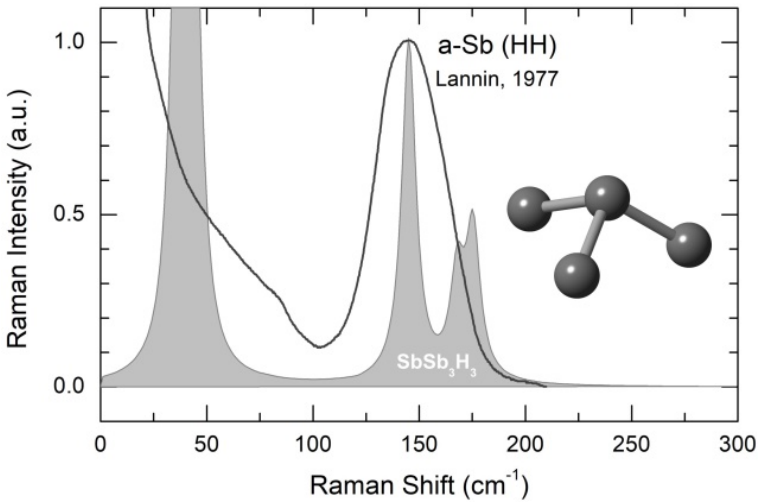

Fig. S2 Raman spectrum of amorphous antimony *a*-Sb thin film[s1] and DFT replica of $SbSb_3H_3$ pyramidal cluster, shown in the insert. The terminal hydrogen species are omitted, and H-related vibrations are removed from the DFT spectrum.

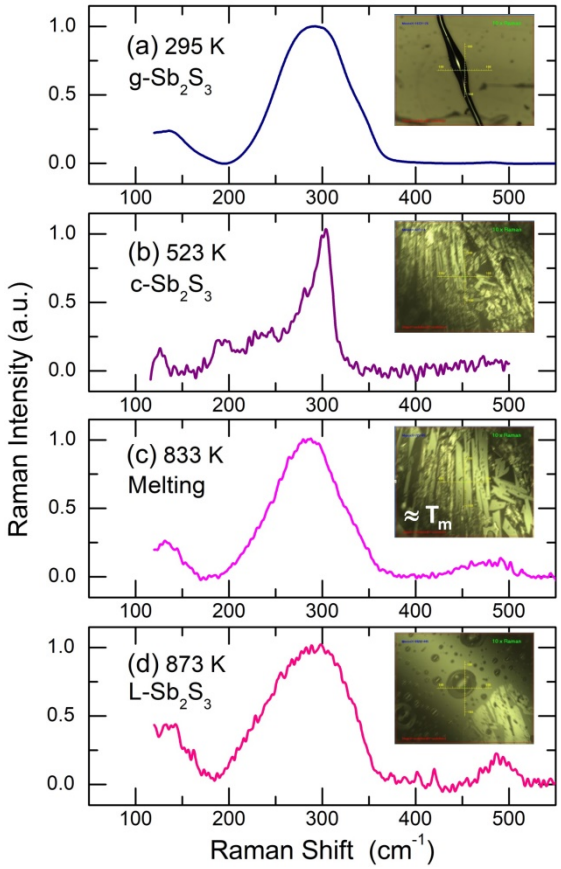

Fig. S3 Evolution of Raman spectra for Sb_2S_3 as a function of temperature: (a) glassy antimony sesquisulfide at room temperature, (b) crystalline Sb_2S_3 at 523 K, (c) partially melted Sb_2S_3 at 833 K, (d) liquid Sb_2S_3 at 873 K. The inserts show microscopic images of the sample at indicated temperatures. The image in (c) represents Sb_2S_3 just before melting.

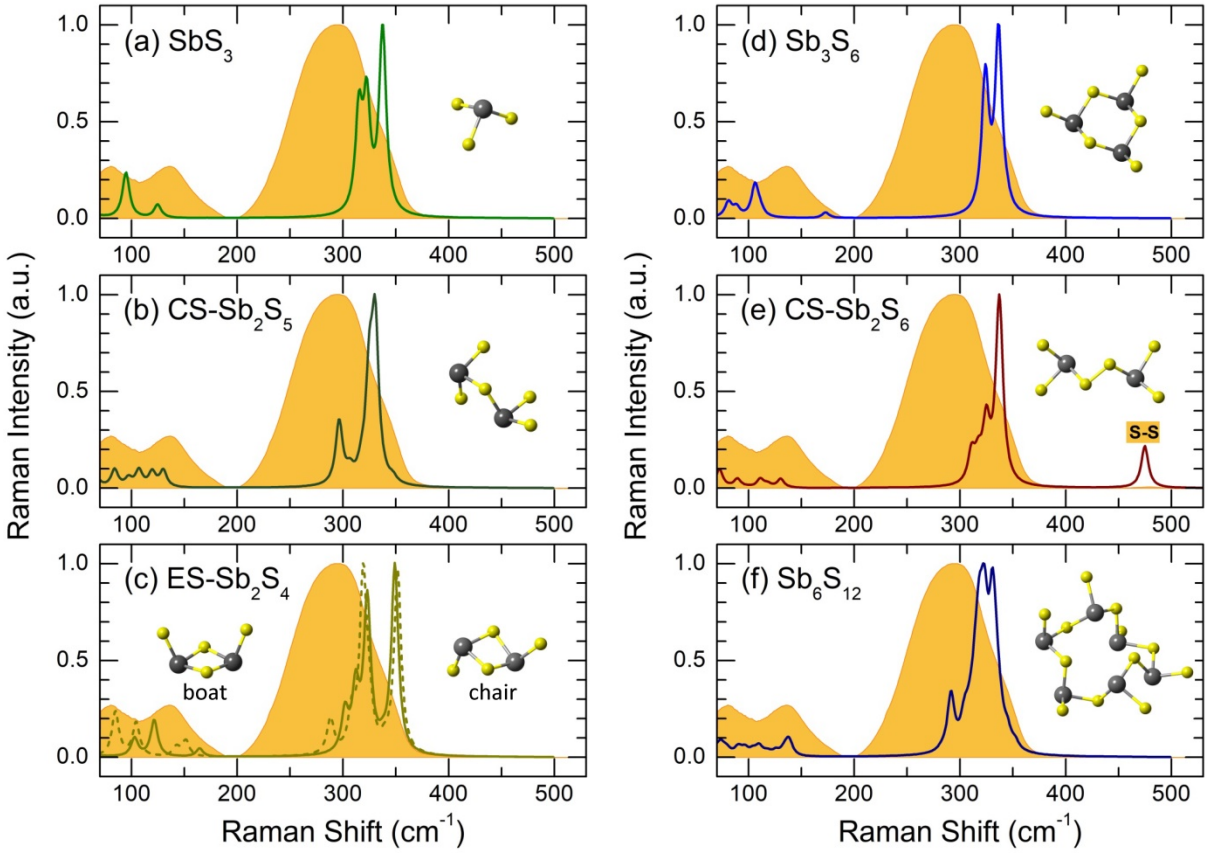

Fig. S4 DFT Raman spectra of size-limited clusters: (a) SbS_3H_3, (b) corner-sharing dimer CS-$Sb_2S_5H_4$, (c) edge-sharing dimer ES-$Sb_2S_4H_2$ in chair (the solid line) and boat (the dashed line) conformations, (d) $Sb_3S_6H_3$ ring, (e) CS-$Sb_2S_6H_4$ dimer with S-S homopolar bond, (f) $Sb_6S_{12}H_6$ ring, in comparison with experimental Raman spectrum of glassy Sb_2S_3 (highlighted in yellow for all panels). The DFT-optimized clusters are shown in the inserts. The terminal hydrogen species are omitted, and H-related vibrations are removed from the spectra.

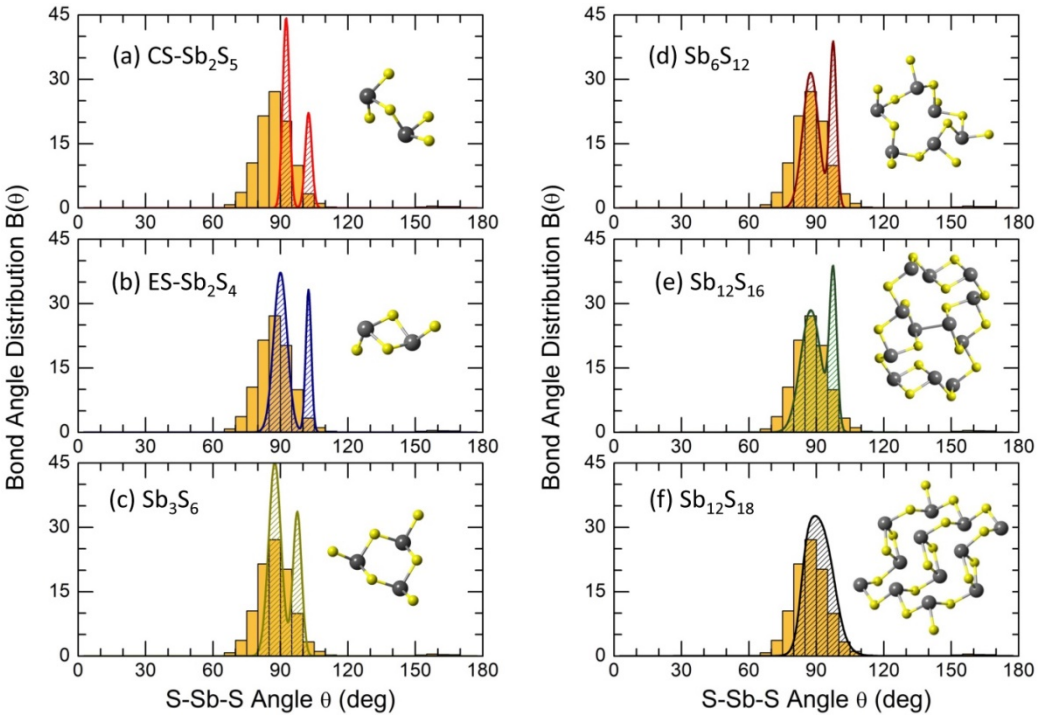

Fig. S5 S-Sb-S bond angle distributions $B(\theta)$ for DFT-optimized clusters: (a) CS-$Sb_2S_5H_4$, (b) ES-$Sb_2S_4H_2$ in chair conformation, (c) $Sb_3S_6H_3$ ring, (d) $Sb_6S_{12}H_6$ ring, (e) $Sb_{12}S_{16}$ and (f) $Sb_{12}S_{18}H_{12}$ entities, originating from modified ribbons $(Sb_4S_6)_\infty$,[s2] in comparison with $B_{SSbS}(\theta)$, derived using first-principles molecular dynamics simulation of g-Sb_2S_3 and highlighted in yellow for all panels.

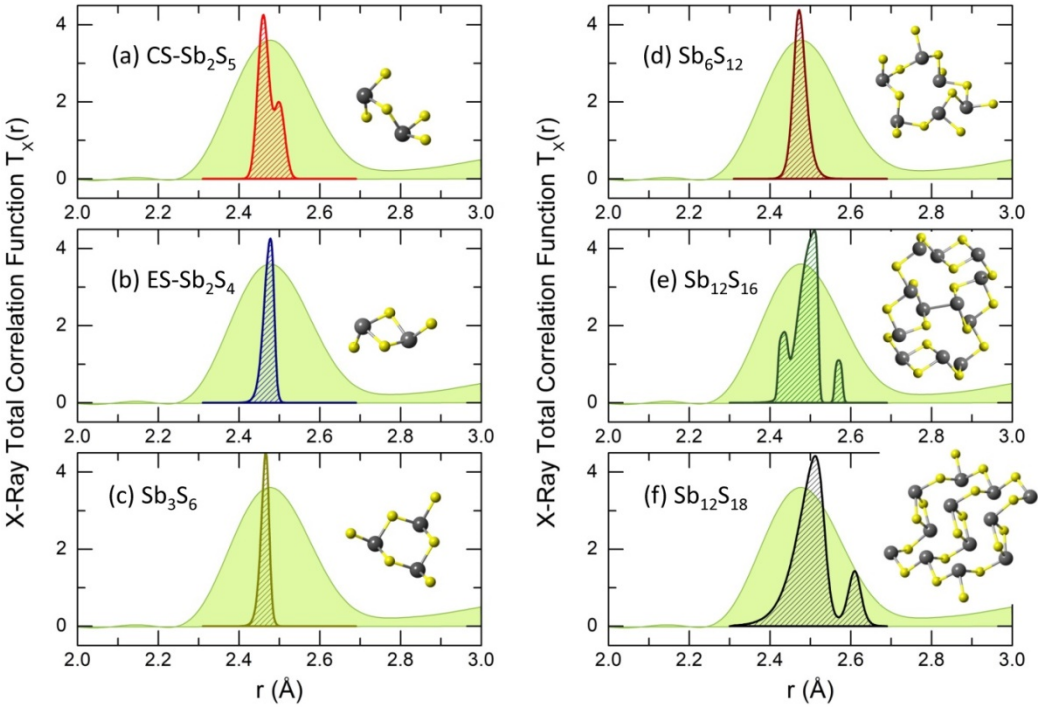

Fig. S6 Distributions of Sb-S interatomic distances in DFT-optimized clusters: (a) CS-$Sb_2S_5H_4$, (b) ES-$Sb_2S_4H_2$ in chair conformation, (c) $Sb_3S_6H_3$ ring, (d) $Sb_6S_{12}H_6$ ring, (e) $Sb_{12}S_{16}$ and (f) $Sb_{12}S_{18}H_{12}$ entities, originating from modified ribbons $(Sb_4S_6)_\infty$, in comparison with derived Sb-S nearest neighbor distances in glassy Sb_2S_3, obtained using high-energy X-ray diffraction and highlighted in light green for all panels.

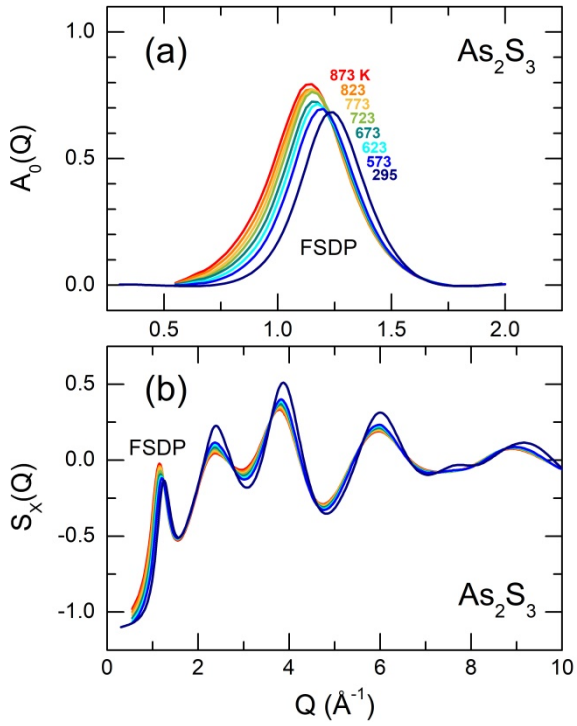

Fig. S7 High-energy X-ray diffraction data in Q-space for glassy and liquid As_2S_3: (a) isolated first sharp diffraction peak (FSDP) and (b) X-ray structure factor $S_X(Q)$ over a limited Q-range as a function of temperature between 295 and 873 K.

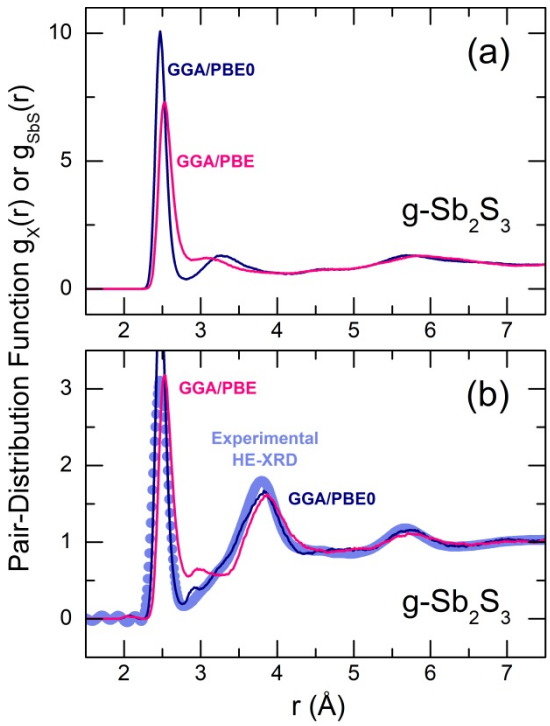

Fig. S8 Comparison of FPMD modeling with standard PBE and hybrid PBE0 functionals: (a) partial Sb-S pair-distribution functions $g_{Sb-S}(r)$, (b) experimental X-ray pair-distribution function $g_X(r)$ and their FPMD replicas. The dark blue line corresponds to PBE0, the pink solid line to PBE in the both panels; the experimental data are shown by the light blue circles.

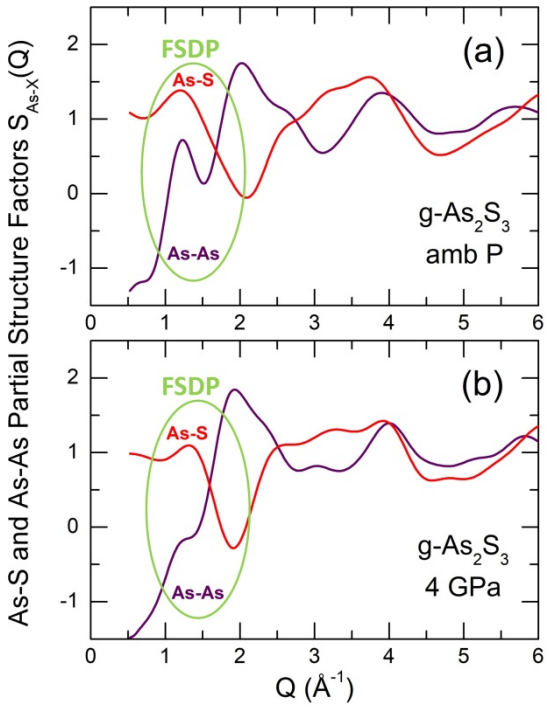

Fig. S9 FPMD modeling of glassy As_2S_3 under high-pressure[s3] using hybrid functional GGA/PBE0 (our preliminary results): (a) As-S and As-S partials structure factors $S_{ij}(Q)$ at ambient pressure, (b) $S_{AsAs}(Q)$ and $S_{AsS}(Q)$ at 4 GPa. The FSDP Q-range is emphasized by the light-green ellipse.

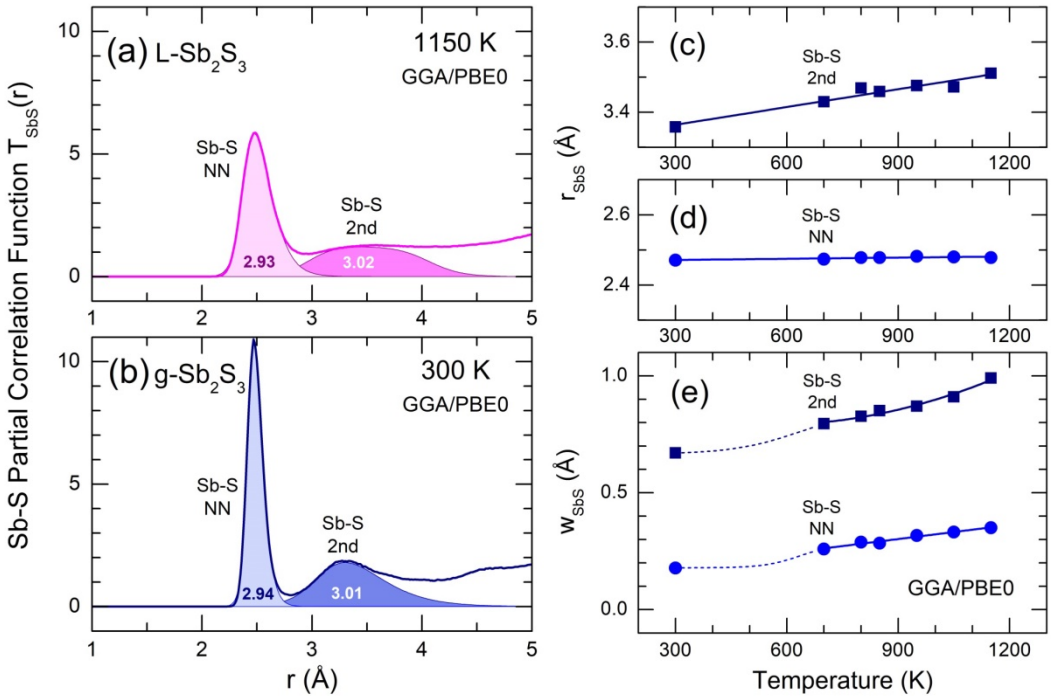

Fig. S10 Fitting Sb-S partials $T_{Sb-S}(r)$ with asymmetric functions at (a) 1150 K, and (b) 300 K; the Sb-S NN peaks are light-colored, the Sb-S second neighbor peaks are dark colored; the derived coordination numbers are also indicated; interatomic distances as a function of temperature: (c) Sb-S second neighbors, (d) Sb-S nearest neighbors; (e) temperature dependence of Sb-S correlation width $w_{Sb-S}(T)$.

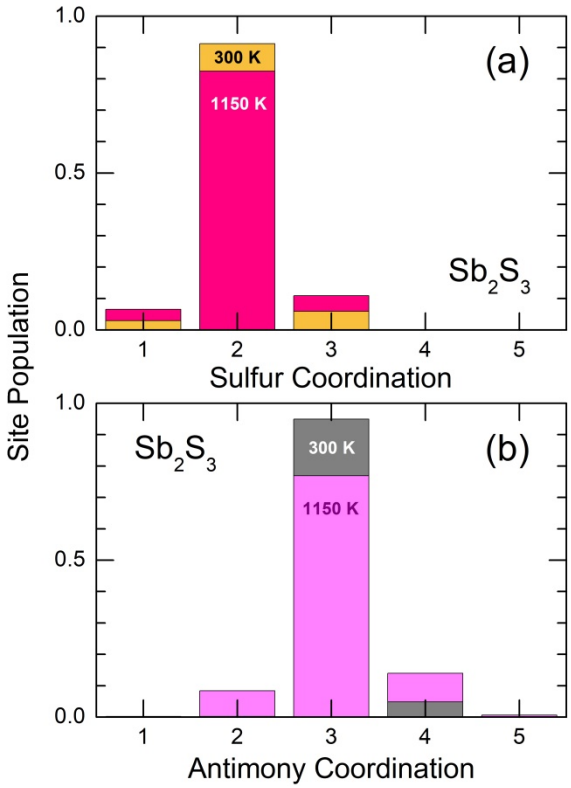

Fig. S11 Coordination distributions of (a) sulfur and (b) antimony at 300 K and 1150 K, derived from the FPMD simulations of Sb_2S_3 using hybrid functional GGA/PBE0.

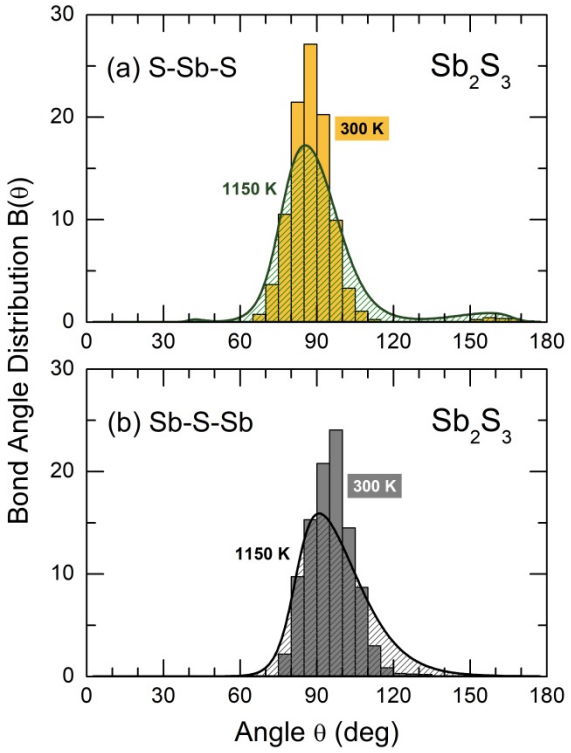

Fig. S12 Bond angle distributions (a) $B_{\mathrm{SSbS}}(\theta)$ and (b) $B_{\mathrm{SbSSb}}(\theta)$ in glassy and liquid Sb_2S_3 at 300 K and 1150 K, respectively.

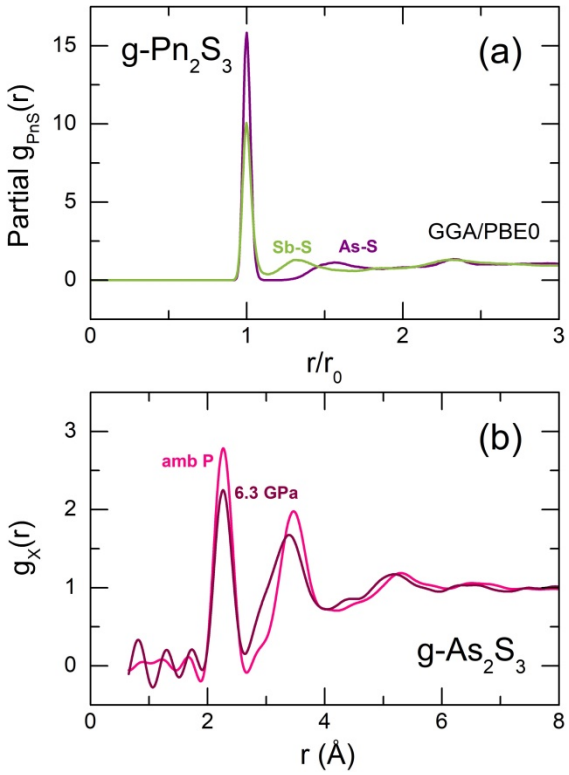

Fig. S13 (a) FPMD partial pair-distribution functions $g_{\mathrm{PnS}}(r)$ for g-Pn_2S_3, Pn = As, Sb; (b) experimental $g_{\mathrm{X}}(r)$ for g-As_2S_3 at ambient pressure and 6.3 GPa;[s3] broader NN and 2ndN peaks of $g_{\mathrm{X}}(r)$ are related to a smaller accessible Q-range in a diamond anvil cell experiment, Q_{max} = 16 Å^{-1} instead of usual 25-30 Å^{-1}.

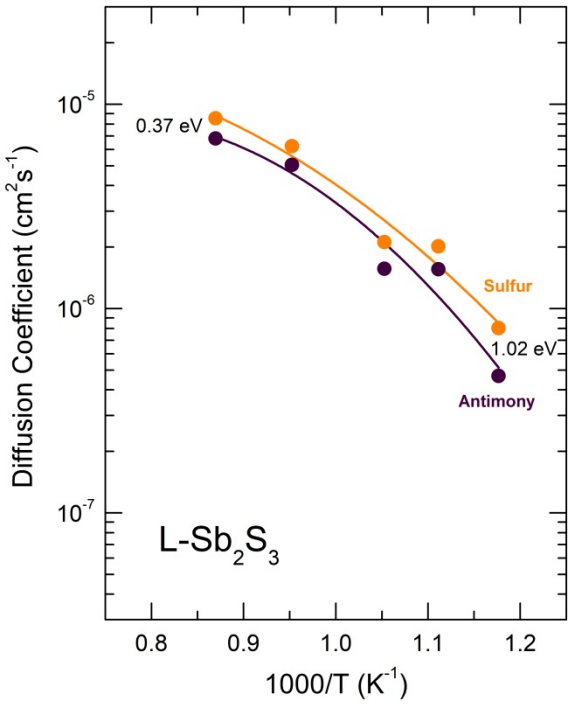

Fig. S14 Derived diffusion coefficients $D_{\mathrm{Sb}}(T)$ and $D_{\mathrm{S}}(T)$ plotted on Arrhenius scale. The effective activation energies in the vicinity of 850 K (1.02 eV) and 1150 K (0.37 eV) are also shown.

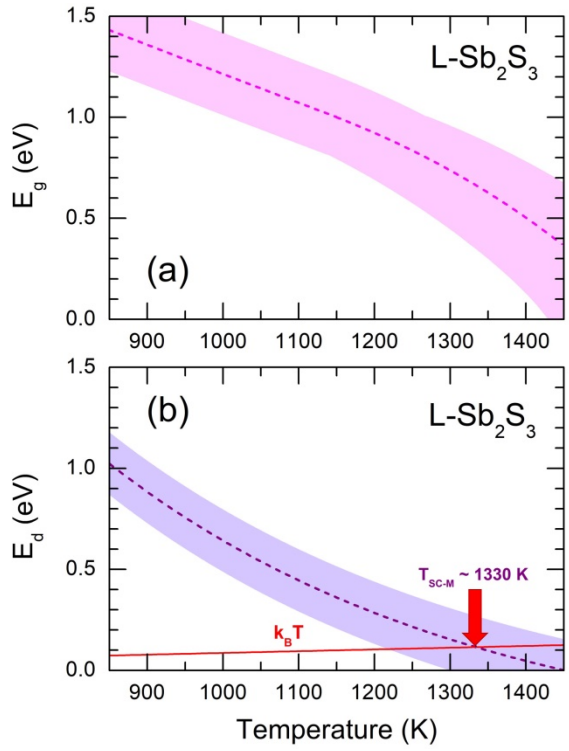

Fig. S15 FPMD estimation of the SC-M transition temperature $T_{\mathrm{SC-M}}$ for liquid Sb_2S_3; (a) bandgap E_g as a function of temperature; (b) atomic diffusion activation energy E_d as a function of temperature. The average thermal energy $k_B T$ is also shown in (b). The effective diffusion coefficient $D_{\mathrm{eff}} = 0.4D_{\mathrm{Sb}} + 0.6D_{\mathrm{S}}$ was taken for these calculations.

Usually, the electronic conductivity increases and bandgap decreases going down on the Periodic Table. Vitreous, crystalline and liquid As_2S_3 and Sb_2S_3 are consistent with this trend. The room temperature conductivity of g-Sb_2S_3 is higher by three orders of magnitude compared to arsenic sesquisulfide, and the difference in E_g is about $\Delta E_g \approx 0.3$ eV. A semiconductor – metal (SC–M) transition is suggested to occur in these two high-T liquids. Using the extrapolation of the optical absorption data,[s4] the SC–M transition is expected at $T_{\mathrm{SC-M}}$ = 1600±150 K for L-As_2S_3[s5] and between 1250 and 1550 K for its antimony counterpart. The last estimation was based on FPMD modeling of the bandgap as a function of temperature or derived from the computed atomic diffusion coefficients, Fig. S15.

The bandgap calculations using the hybrid functional GGA/PBE0 in the metallic limit yields a significant uncertainty in $T_{\mathrm{SC-M}}$ = 1550±120 K. As expected, the modeling with the standard functional GGA/PBE reveals a metallic liquid at lower temperature, 1250±75 K. The derived $T_{\mathrm{SC-M}}$ values seem to be the two extremes for estimation of a SC-M transition using the electronic properties. Another alternative gives the atomic dynamics suggesting that the diffusion activation energy E_d in the metallic fluid appears to be comparable with the average thermal energy, $E_d \approx k_B T$. This alternative yields $T_{\mathrm{SC-M}}$ = 1330±100 K, which corresponds to a change in the slope of E_g(PBE0), Fig. S15(a). Finally, liquid Sb_2S_3 exhibits the metallic conductivity above approximately 1300-1500 K.[s6]

Additional references

s1 J. S. Lannin, Raman scattering properties of amorphous As and Sb, *Phys. Rev. B*, 1977, **15**, 3863–3871.

s2 P. Bayliss and W. Nowacki, Refinement of the crystal structure of stibnite, Sb_2S_3, *Z. Kristallogr.*, 1972, **135**, 308–315.

s3 E. Soignard, O. B. Tsiok, A. S. Tverjanovich, A. Bytchkov, A. Sokolov, V. V. Brazhkin, C. J. Benmore, and E. Bychkov, Pressure-driven chemical disorder in glassy As_2S_3 up to 14.7 GPa, post-densification effects, and applications in materials design, *J. Phys. Chem. B*, 2020, **124**, 430–442.

s4 S. Hosokawa, Y. Sakaguchi, H. Hiasa, and K. Tamura, Optical absorption spectra of liquid As_2S_3 and As_2Se_3 over a wide temperature range, *J. Phys.: Condens. Matter*, 1991, **3**, 6673–6677.

s5 S. Wei, P. Lucas and C. A. Angell, Phase-change materials: the view from the liquid phase and the metallicity parameter, *MRC Bull.*, 2019, **44**, 691–698.

s6 V. A. Alekseev, A. A. Andreev and M. V. Sadovskiĭ, Semiconductor-metal transition in liquid semiconductors, *Sov. Phys. Usp.*, 1980, **23**, 551–575.